Tautomerization of Phenol at the External Lewis Acid Sites of Scandium-, Iron- and Gallium-Substituted Zeolite MFI

Carlos Hernandez-Tamargo, Alberto Roldan, and Nora H. de Leeuw*

School of Chemistry, Cardiff University, Main Building, Park Place, Cardiff, United Kingdom CF10 3AT

* Supporting Information

ABSTRACT: We have employed density functional theory calculations to analyze the possible tautomerization of phenol mediated by three different Lewis acid sites at the external (10) surface of zeolite MFI. A silicon atom of the silanol group was substituted by Sc, Fe, and Ga metal atoms, which adopted a formal charge of 3+. This substituted silanol was dehydrated in order to form three-coordinated Lewis acid sites. The tautomerization of phenol involves the adsorption of the molecule on the Lewis site, the dissociation of the phenolic O−H bond and the transfer of the proton to the zeolite framework. This proton is transferred from the zeolite to the C atom at ortho positions to the phenolic O atom, thus generating the tautomer. The acidity of the substituted Lewis sites follows a strength order of Ga < Fe < Sc, where the Sc substitution provides the lowest energy barriers: 33 kJ/mol for the dissociation of the O−H bond, and 32 kJ/mol for the formation of the C−H bond, calculated with the GGA functional PBE including Grimme's dispersion corrections. We observed that the GGA functional PBE produces binding energies and energy barriers with a difference of less than 13 kJ/mol compared to the meta-GGA TPSS and rev-TPSS and the hybrid-GGA HSE06.

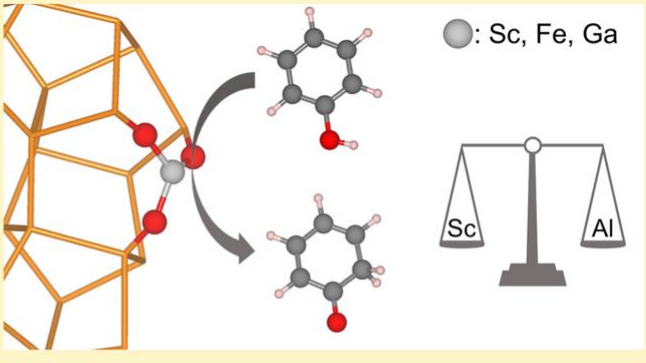

1. INTRODUCTION

The conversion of lignin may provide a sustainable and renewable route to chemicals and fuels. However, the polymeric structure of lignin consists of interlinked phenolic monomers, with high oxygen content, which requires appropriate catalysts to guarantee selectivity and high yields during its processing.[1−3] In the case of fuel-oriented utilization, it is desirable to increase the H:C and C:O ratios of the lignin-derived products in order to improve the efficiency of combustion.[1] Several experimental methods have been designed to depolymerize, deoxygenate and hydrogenate lignin. For instance, the pyrolysis of lignin-derived compounds has been performed in the presence of catalytically active zeolites in order to decrease the oxygen content. However, this method generates a high number of different products without apparent selectivity, and has the drawback of generating solid residues that decrease the lifetime of the catalyst.[4−7] On the other hand, the hydrodeoxygenation (HDO) of organosolv lignin and lignin-derived compounds, using bifunctional catalysts consisting of transition metal nanoparticles deposited on acid supports, outperforms the pyrolytic method in selectivity, yields and a reduction of solid byproducts.[8−11]

The bifunctional catalysts comprise transition metal nanoparticles, which promote the hydrogenation, supported on solid acids that mediate the dehydration and alkylation of the hydrogenation intermediates.[8,12−14] Examples of bifunctional catalysts include Pt supported on zeolite HY (in short Pt/HY),[8] Ru/HZSM-5,[10] Ni/HZSM-5, and Ni/HBEA,[11] as well as a combination of Pd/C and zeolite HZSM-5.[9] A mixture of monocyclic and bicyclic alkanes are obtained with these methods, highlighting the dehydration function of the support and the hydrogenation by the metallic component.

The HDO of phenolic monomers, such as phenol and cresol, have been the subject of extensive research, both experimental and theoretical, because they are good examples of the major recalcitrant species derived from the upgrading of lignin.[15−19] The modifications occurring to the phenolic species depend on the metal and support. For example, 3-methylcyclohexanone is the main product of the processing of m-cresol on Ni/SiO_2 or Pt/SiO_2, while selectivity toward toluene is highest when the conversion takes place on Fe/SiO_2 or Pt/ZrO_2.[17,18] This outcome has been explained by the occurrence of keto−enol tautomerism (represented in Figure 1) that transforms m-cresol into 3-methyl-3,5-cyclohexadie-none. The cyclohexadienone may follow two different pathways: (i) hydrogenation of the C C bonds, producing 3-methyl-cyclohexanone or (ii) the hydrogenation of the C O group followed by dehydration, generating toluene.[17,18] However, recent DFT calculations have shown that the most probable pathway to obtain toluene consists of the direct deoxygenation of m-cresol, promoted by the oxophilicity of the

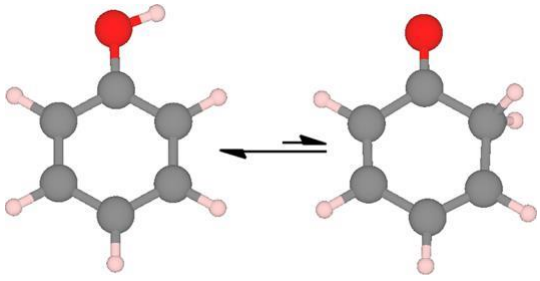

Figure 1. Representation of the tautomerization of phenol.

metal particle's surfaces, such as Ru(0001);[19] this logic could also be applied to the selectivity observed on oxophilic supports such as ZrO_2.[17,20] Nevertheless, the keto−enol tautomerism is still an appropriate approach to explain the product selectivity of the hydroprocessing, especially when there are no oxophilic components within the catalysts.[17−20]

Considering the importance of the keto−enol tautomerization during the hydroprocessing, we have performed a computational study of the possible isomerization of phenol on zeolite Socony Mobil-five (MFI)[21−23] doped with different metal atoms, which is based on the wide utilization of this zeolite as a support during the HDO of lignin-derived compounds. Computer simulations, using either quantum mechanics or classical methods, have provided crucial insights into the physical and chemical properties of zeolites. For example, calculations of aluminum siting and substitution configurations have complemented experimental techniques, such as nuclear magnetic resonance.[23− 25] Furthermore, the analysis of proton transfer in zeolites is important owing to their solid acid character, and computer modeling has been essential in providing understanding of this process at the atomic level.[26−30] The elucidation of the adsorption configurations and reaction pathway in the transformation of environmentally and industrially important molecules inside the pore system of zeolites is another area, where theoretical predictions have been extremely valuable.[30−33] The present work falls under this latter topic.

Previously, we have shown that three-coordinated Lewis acid sites in aluminum-substituted zeolite MFI reduce by at least four times the activation energy of phenol tautomerization compared to direct isomerization in the gas phase.[34] In the present work, we have extended this study in order to consider other dopants with a formal charge of 3+. Experimental intraframework substitutions of zeolites with Sc, Fe and Ga have been reported, and thus we have used these metals to study the tautomerization of phenol on their Lewis acid forms.[35−37] We have placed these Lewis acid sites at the external surface of the zeolite, where they are more easily accessible to medium-sized molecules, such as phenol. Incidentally, recent experimental reports on Pt nanoparticles confined in the cavities of zeolite-A have shown the importance of the external Lewis acid sites for the adsorption and hydrogenation of unsaturated molecules through a hydrogen spillover mechanism.[38−40] Zeolite A (framework type LTA) and zeolite MFI have different pore dimensions: while LTA is characterized by eight-membered ring (8MR) pore apertures,[41] effectively hindering the diffusion of molecules such as phenol into its pore system, MFI shows 10MR openings, which does allow the access of phenol to the interior of the zeolite. However, in the present work, we have exclusively analyzed the adsorption of phenol at the external surface of zeolite MFI.

Our choice is based on the size of the metal nanoparticles, with diameters larger than 2 nm,[12,42] which therefore cannot diffuse into the pore system of the zeolite and can only be supported at the outer surface of the microporous material. In addition, the selectivity and pathway during hydroprocessing have been ascribed to the synergy that occurs at the metal−support interface.[20,43] Hence, Lewis acid sites located at the external surface of the zeolite and at close distance from the metal clusters should have an important role to play in the HDO process.

The first part of the discussion is dedicated to the formation of three-coordinated Lewis acid sites resulting from the dehydration of metal-substituted silanol groups at the external surface of zeolite MFI. It is followed by the adsorption of phenol and the analysis of its proficiency to substitute water at the Lewis site. Then, the tautomerization is discussed on the basis of a three-step process that involves (i) dissociation of the O−H bond of phenol, (ii) rotation of the aromatic ring, and (iii) formation of the C−H bond following the transfer of the phenolic H back to the molecule.[34] A similar pathway has been proposed for the tautomerization of phenol and m-cresol on the surfaces Pt(111), Pd(111), and Ru(0001).[19,44] A comparison between GGA, meta-GGA, and hybrid-GGA functionals is also discussed and rationalized, which measures the precision of the GGA compared to higher tier functionals with increased accuracy.

2. COMPUTATIONAL METHODS

2.1. DFT Calculations. We have employed density functional theory (DFT) methods to perform all calculations presented in this work, as implemented in the Vienna Ab-Initio Simulation Package (VASP).[45−48] We have used the derivation of Perdew, Burke, and Ernzerhof (PBE) of the general gradient approximation (GGA) to obtain the exchange-correlation energy of the systems.[49] Although most of the calculations presented in this work were generated using the GGA functional PBE, we have also used the GGA functional PBE optimized for solids (PBEsol),[50,51] the meta-GGA functional proposed by Tao, Perdew, Staroverov, and Scuseria (TPSS)[52] and its revised version (rev-TPSS),[53] and the hybrid functional proposed by Heyd, Scuseria, and Ernzerhof (HSE06),[54,55] to compare and validate the results generated by PBE. We observed that the PBE functional produced binding energies and energy barriers with differences no bigger than 13 kJ/mol compared to the values calculated by the higher tier functionals; for more information see section S1 of the Supporting Information, where the data derived from PBEsol, TPSS, rev-TPSS, and HSE06 are compiled. The PBE functional was accompanied by the Grimme method (DFT-D3) to include the long-range dispersion forces.[56−59] This approach incorporates first-principle computing and geometry information into the parametrization of the pairwise coefficients and cutoff radii, as well as three-body terms to avoid the overestimation of the attractive forces. A basis set of plane waves was used to describe the valence electrons, employing the projector-augmented-wave method (PAW) to account for the nodal features of the valence wave functions and their interaction with the inner part of the atoms.[60,61] The precision of the basis set was assured by a plane wave kinetic energy cutoff of 550 eV. The Brillouin zone was only sampled with the Gamma point considering the large size of the supercell under study. Gaussian smearing of the electronic states was employed to improve the self-consistent field

convergence, with band widths of 0.01 and 0.1 eV for isolated molecules (water and phenol) and zeolite MFI (with and without adsorbate), respectively.[62,63] During the geometry optimization, we adopted the thresholds 10^{-5} eV and 0.03 eV/Å as fair convergence criteria for the electronic and ionic relaxations, respectively. All calculations were performed under spin polarization conditions.

In the case of the Fe-substituted zeolite, we performed two sets of calculations: the first one used Dudarev's approach[64,65] to deal with the electron correlation, which is derived from the on-site Coulomb repulsion of the 3d electrons of the Fe atom, whereas we did not use this approach in the second set of calculations. We employed a value of 4.0 eV for U_{eff} in accordance with previous reports of different iron oxides.[66,67] The calculations without on-site Coulomb correction were used together with the results for Sc- and Ga-substituted zeolites to discuss the structural features along the tautome-rization pathway.

The molecular binding free energy was calculated with the following equation:

$$F_{Bind.} = F_{molecule/zeolite} - (F_{zeolite} + F_{molecule}^{gas}) \quad (1)$$

where $F_{molecule/zeolite}$ is the free energy of the zeolite with an adsorbed molecule of water or phenol, $F_{zeolite}$ is the free energy of the bare zeolite and $F^{gas}_{molecule}$ is the free energy of a molecule of water or phenol in the gas phase; we considered as the gas phase an isolated molecule in a box with dimensions 20 × 21 × 22 $Å^3$. The free energies were computed by including the zero-point energy correction and the entropic contributions at 473 K; this temperature is a reasonable representation of the array of values normally used in hydroprocessing experiments.[9,12,13,68] Only the vibrational entropy was considered for the zeolite-related systems, while the rotational and translational entropies were also computed for the molecules in the gas phase, assuming them as ideal gases. The vibrational frequencies were calculated by the finite difference method, using small enough displacements to keep the system within the harmonic approximation. During the vibrational calculations, we only allowed atomic displacements for the metal substituent, the first-neighbor SiO_4 tetrahedra surrounding the metal and the molecule adsorbed on the Lewis acid site. This constraint was introduced to speed up the calculations without introducing serious errors.[34] The derived thermodynamic quantities (thermal energies, enthalpies, entropies and free energies) are reported in section S2 of the Supporting Information.

The energy barriers along the reaction pathways were calculated by combining the nudged elastic band (NEB) method and the improved dimer method (IDM).[69−72] We tested from one to three images between reactants and products to perform the transition state (TS) geometry optimization under the NEB algorithm. We found that the utilization of a single image was enough to start the exploration of the TS. Thereafter, the output of the NEB calculation was used as a reasonable TS guess structure, which was refined by the IDM. During the search of the TS, only the metal substituent, the three SiO_4 tetrahedra binding the metal, and the phenol or water molecule adsorbed on the Lewis site were allowed to relax, the rest of the structure was kept frozen. We adopted this scheme because the freedom of movement that phenol retains while it is adsorbed makes the relaxation of the TS less dependent on the long-range flexibility of the framework. The reactant and product of each reaction step were optimized without geometry constraints. This procedure increases considerably the speed of the search for the TS, mainly during the frequency calculations needed for the IDM, which incurs in an overestimation of the energy barriers of less than 4 kJ/mol compared to the systems without constraints.

2.2. Simulation Model. All simulations were carried out using periodic boundary conditions. The input coordinates and unit cell of zeolite MFI, which were used for the geometry optimization, were obtained from the database of the International Zeolite Association.[73] We optimized the unit cell by creating a set of fixed volume calculations, allowing the atomic positions and the cell shape to relax. Afterward, the correlation between the energies of the cells and their volumes was fitted to the Birch−Murnaghan equation of state.[74] This procedure avoids the drawbacks related to the Pulay stress,[75] and gives the bulk modulus as an adjustable parameter. The relaxed equilibrium cell had values of 20.272, 19.942, and 13.400 Å for the parameters a, b, and c, respectively, with a volume of 5417 $Å^3$, which was less than 1% larger than the experimental value.[76] At the same time, we calculated a bulk modulus of 18.4 GPa, in good agreement with an experimental measurement of 18.2 GPa.[76]

We have used the slab model to analyze the adsorption of phenol at the (010) surface of zeolite MFI, which is the exposed face in MFI nanosheets.[25,77] The slab was built by cutting the structure along the [010] direction and keeping the periodicity over the (010) plane, saturating the cleaved Si−O bonds with hydroxyl groups. This procedure to create the slab resembles the methodology of previous computational simulations, where the external surfaces of zeolites have been considered explicitly.[78−81] This type of morphology has been experimentally synthesized in the form of single unit cell nanosheets.[77] In previous publications, we have shown that the external surface of zeolite MFI is well-described by a slab formed by one pentasil layer,[34] which closely resembled the results obtained using a more realistic slab constituted of two pentasil layers.[25,30] Therefore, we have used one-pentasil slabs in this work, placing a vacuum layer of 20 Å along the normal direction to the surface in order to minimize the interaction between periodic images, leading to unit cell parameters for the slab model of 20.272, 34.971, and 13.400 Å along the a, b and c directions, respectively.

Studying the Al substitution of the T-sites in a one-pentasil slab, we observed that the T9 site, which is shown in Figure 2, was the most stable Al-substituted silanol out of four different available positions per unit cell: T7, T9, T10, and T12.[34] Therefore, we have used this site to substitute Sc, Fe, and Ga and compare them to our previous results on the tautomerization of phenol on Al-substituted MFI.

The visualization of all structures shown in this work was obtained with the code Visualization for Electronic and Structural Analysis (VESTA 3).[82]

3. RESULTS AND DISCUSSION

3.1. Formation of the Lewis Acid Sites. A spare negative charge is introduced within the zeolite framework after the metal atoms Sc, Fe and Ga, with a formal charge of 3+, substitute a Si atom. A Brønsted acid is generated when this negative charge is neutralized by H^+ upon ion-exchange with NH_4^+ followed by calcination. Substituted silanol groups at the external surface of zeolites are the precursors of three-coordinated Lewis acid sites.[25,78] These Lewis acids are produced following the transfer of the acidic H^+ to the OH

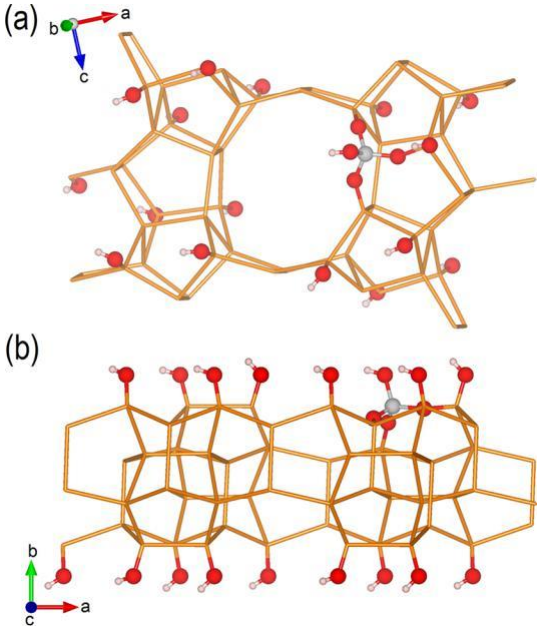

Figure 2. Representation of the (010) surface of zeolite MFI: (a) top and (b) lateral views. The T9 site is represented in light gray, silanol O atoms in red, H in white, and Si by orange sticks.

group of the metal-substituted silanol with the subsequent formation of water, as shown in Figure 3. In the present study,

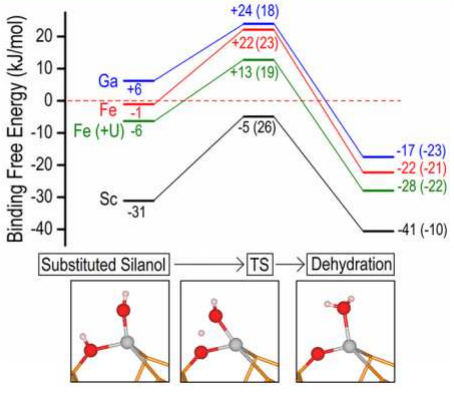

Figure 3. Binding free energies along the dehydration pathway of three metal-substituted silanols: Sc (black line), Fe (red line), Fe with the +U correction (green line), and Ga (blue line). The barrier and reaction energies are shown within parentheses. The horizontal dashed line marks the reference energy (shifted to zero), constituted by the bare Lewis acid site and a molecule of water in the gas phase. Close-ups showing the relevant structural features along the dehydration pathway are presented at the bottom of the graph. The T9 site is represented in light gray, silanol and acidic O atoms in red, H in white, and Si by orange sticks.

this transformation is exothermic, releasing energies of 10, 21, and 23 kJ/mol, and overcoming small energy barriers of 26, 23, and 18 kJ/mol for substitutions with Sc, Fe, and Ga, respectively (see Figure 3). The inclusion of the on-site Coulomb correction (hereafter referred as +U) for Fe decreased the absolute energy of the reactant, TS and product by 5 to 7 kJ/mol, yielding an exothermic energy of 22 kJ/mol and a barrier of 19 kJ/mol, thus retaining the trends of the calculation without +U. The activation energies in Figure 3 are similar to the equivalent transformation for Al-substituted silanol T9, where values between 10 and 20 kJ/mol have been calculated.[25] Thus, we can conclude that the dehydration of the metal-substituted silanols is thermodynamically and kinetically favored.

The water molecule is desorbed from the Lewis acid site upon thermal treatment of the material, leading to the generation of three-coordinated M^{3+} centers.[83] Therefore, we have used the bare three-coordinated Lewis centers, shown in Figure 4, as reference structures to calculate the binding free energies along the tautomerization process.

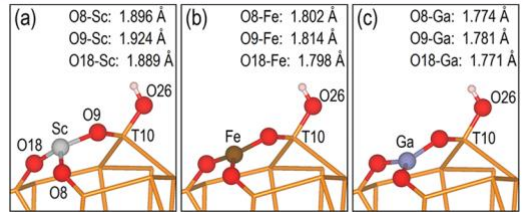

Figure 4. Optimized, three-coordinated Lewis acid sites after dehydration and water desorption of substituted silanol T9. Important O atoms are represented in red, H atoms in white, Sc atom in light gray, Fe atom in brown, Ga atom in light blue, and Si by orange sticks. Relevant interatomic distances are shown for each geometry.

3.2. Adsorption of Phenol. Two different configurations were examined for the adsorption of phenol on the Lewis sites: the nonplanar configuration, which places the plane of the aromatic ring perpendicular to the plane created by the three framework O atoms that bind the metal substituent (see Figure 5a), and the coplanar configuration, which places the plane of the aromatic ring almost parallel to the plane created by the three framework O atoms (see Figure 5b).

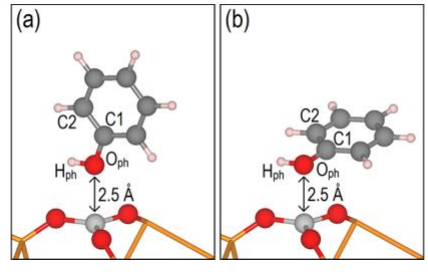

Figure 5. Representation of the adsorption of phenol with (a) nonplanar and (b) coplanar configurations before geometry optimization. Important O atoms are represented in red, C atoms in dark gray, H atoms in white, metal substituent in light gray, and Si by orange sticks.

Phenol adsorbs preferentially on the three Lewis acid sites with a coplanar configuration, as indicated by the calculated binding free energies of −34, −14, and −6 kJ/mol against values of −7, +11, and +17 kJ/mol for the nonplanar configuration on the Sc, Fe, and Ga sites, respectively. The +U approach reduced the stability of the bare, Fe-substituted Lewis acid site, and thus increased the strength of the adsorption by 5−6 kJ/mol. These results agree with the preferential coplanar adsorption of phenol on Al-substituted zeolite MFI, which is 30 kJ/mol stronger than the nonplanar configuration.[34]

The binding energy has been identified as a convenient descriptor to characterize the Lewis acidity in zeolites.[84] Consequently, according to the values of binding free energies

Table 1. Bader Atomic Charges Calculated with the Functionals PBE and HSE06

	PBE					HSE06				
M	q(M)[a]	q(ph)[b]	q(M)[c]	q(3O)[d]	q−/q+[e]	q(M)[a]	q(ph)[b]	q(M)[c]	q(3O)[d]	q−/q+[e]
Al	+2.445	+0.034	+0.024	−0.014	0.24	+2.484	+0.040	+0.017	−0.013	0.23
Sc	+2.025	+0.072	+0.009	−0.049	0.60	+2.147	+0.067	+0.008	−0.046	0.61
Fe	+1.639	+0.113	+0.030	−0.099	0.69	+1.853	+0.094	+0.031	−0.090	0.72
Fe (+U)	+1.759	+0.102	+0.032	−0.094	0.70	–	–	–	–	–
Ga	+1.847	+0.102	+0.050	−0.118	0.78	+1.955	+0.096	+0.040	−0.101	0.74

[a]q(M): Bader atomic charges (e^- units) of the Al, Sc, Fe, and Ga atoms before the adsorption of phenol. [b]q(ph): Total charge of phenol after adsorption. [c] q(M): Variation of q(M) after the adsorption of phenol. [d] q(3O): Variation of the total charge of the three O atoms that bind the metal substituent after the adsorption of phenol. [e]q−/q+: Ratio between the negative and positive charges, calculated using eq 4.

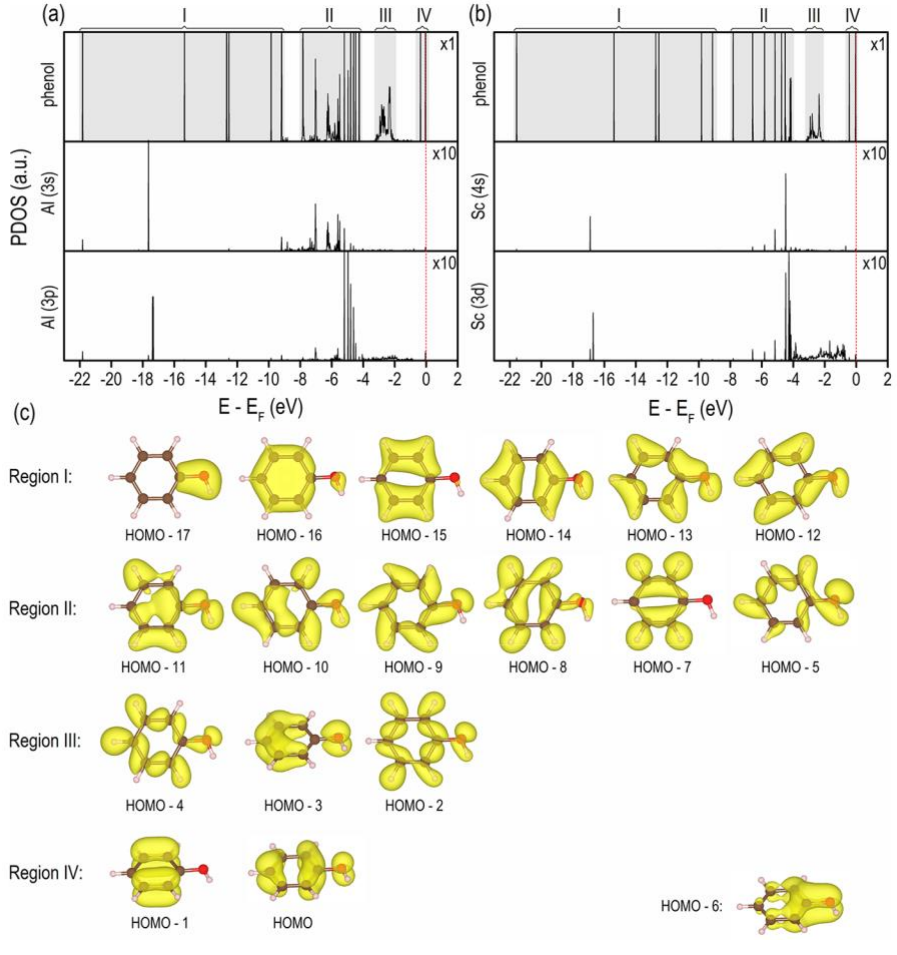

Figure 6. Projected density of states (PDOS) of (a) Sc-substituted and (b) Al-substituted MFI nanosheet: (top graphs) total projection onto phenol atoms, (middle graphs) projection onto the 3s orbitals of Al and the 4s orbitals of Sc, and (bottom graphs) projection onto the 3p orbitals of Al and the 3d orbitals of Sc. (c) Molecular orbitals (MO) of phenol within each of the four regions shadowed in light gray in the PDOS profiles of phenol. The MO HOMO−6 was not detected within any of the four regions, and we reason that it was rehybridized with the rest of the MO after adsorption.

calculated in this work, combined with the results of phenol adsorption on Al-substituted zeolite MFI,[34] we can establish the following order of Lewis acid strength: Ga < Fe < Sc < Al.

We have used the Bader atomic charges[85−88] to analyze the charge transfer between phenol and the Lewis acid sites, compiling the values derived by PBE and HSE06 in Table 1. In the case of HSE06, the PBE-optimized geometries were used as input coordinates for single-point calculations. Before adsorption of phenol, the charge of the metal centers q(M) yielded by PBE followed the order: Fe (+1.639 e^- and +1.759 e^- with the +U correction) < Ga (+1.847 e^-) < Sc (+2.025 e^-) < Al (+2.445 e^-), which almost correlates with the ranking of adsorption energies except for the Fe−Ga swap at the beginning of the series; HSE06 produced similar results.

After adsorption of phenol, the variation of the atomic charges was calculated with the following equations:

$$q(\mathrm{M}) = q(\mathrm{M})_{after\ ads.} - q(\mathrm{M})_{before\ ads.} \quad (2)$$

$$q(3\mathrm{O}) = q(3\mathrm{O})_{after\ ads.} - q(3\mathrm{O})_{before\ ads.} \quad (3)$$

$$q-/q+ = \left| \frac{q(3O)}{q(M) + q(ph)} \right| \quad (4)$$

where q(M) is the variation of the metal atomic charge q(M) before and after the adsorption of phenol, q(3O) is the variation of the total atomic charge of the three O atoms q(3O) that bind the metal before and after the adsorption of phenol, and $q-/q_+$ is the ratio between the variations in negative and positive charges after adsorption, including the charge of phenol q(ph). This ratio provides an indication of the fraction of the charge that is transferred to the O atoms directly binding the metal (see Table 1).

Upon adsorption of phenol, we observed a net charge transfer from phenol to the zeolite, which, according to PBE and HSE06, increased along the series Al < Sc < Fe ≈ Ga. However, despite this net movement of electronic charge into the zeolite framework, the positive charge of the metal centers increased after the interaction with phenol, with Sc reporting the smallest variation q(M) (PBE: + 0.009 e^- and HSE06 + 0.008 e^-), followed by Al and Fe, and with Ga yielding the largest growth (PBE: + 0.050 e^- and HSE06 + 0.040 e^-). In the case of Sc, Fe, and Ga, more than half of the net charge transferred from phenol and the metal substituent to the rest of the zeolite was located in the three O atoms binding the metal center, yielding $q-/q_+$ values between 0.60 and 0.80. In contrast, only approximately 20% of this net charge remained in the three O atoms binding the Al atom. We have rationalized these observations as follows: the smaller the electronegativity of the metal the stronger the adsorption energy within the series Sc, Fe and Ga, where the three atoms are in the same row of the periodic table;[89] a similar correlation has been reported before for M^{4+}-substituted zeolite MFI.[84] This relation holds for substitutions with elements in the same group of the periodic table: the electronegativity of Al is lower than Ga, and consequently its adsorption energy is higher. This effect may be related to the capacity of the Lewis acid site to back-transfer part of the electronic charge that is received from phenol. However, when Al is compared to Sc, the opposite trend is observed, Al has a higher electronegativity and also has a stronger adsorption energy than Sc.[34,89] Figure 6 shows the projected density of states (PDOS) onto the valence states of Al and Sc, where we have observed differences in their hybridization state with phenol.

The PDOS of adsorbed phenol can be divided into four regions that span approximately from −22 to 0.0 eV, with the Fermi energy shifted to zero, and contain the profiles associated with the molecular orbitals of phenol (see Figure 6). Regions II and III show the strongest signs of hybridization between the molecular orbitals of phenol and the electronic states of Al and Sc. While region III, spanning from approximately −3 to −2 eV, is very similar in Al and Sc, the profile of region II indicates marked differences between the two metal substituents. In the case of phenol on Al, region II shows a strong scattering of the states associated with the molecular orbitals, which is a measure of important electronic hybridization and phenol−Al interaction. On the other hand, in the case of phenol on Sc, region II is mainly characterized by single peaks, suggesting a weaker phenol−Sc interaction. This feature highlights the more efficient hybridization of phenol with the electronic states Al(3s,3p) in comparison to Sc(4s,3d), and thus justifies the stronger binding energy of phenol to Al than to Sc.

We also compared the thermodynamic viability of the coplanar adsorption of phenol against the adsorption of water on the Lewis acid sites, adopting the condition that the translational and rotational degree of freedoms of the physisorbed molecules are frustrated.[90] Therefore, we only included the vibrational contribution to the entropy and the thermic energy in eq 1 for molecules optimized in the gas phase. Under these conditions, and at 473 K, the binding free energies of phenol were stronger than those of water by 31 to 35 kJ/mol for the three metal substitutions. Hence, according to our calculations, the Lewis site preferentially adsorbs phenol over water.

Figure 7 shows the most stable coplanar configurations after geometry optimization. After the adsorption of phenol, the

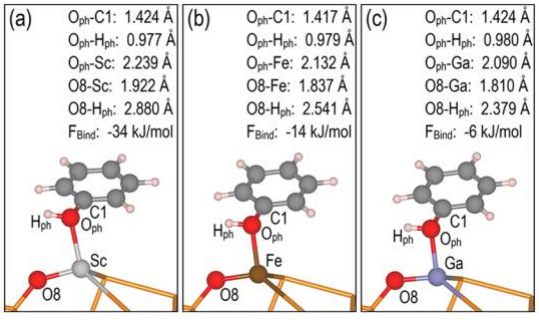

Figure 7. Most stable coplanar adsorptions of phenol on the three Lewis centers after geometry optimization: (a) Sc, (b) Fe, and (c) Ga. Important O atoms are represented in red, C atoms in dark gray, H atoms in white, and Si by orange sticks. Relevant interatomic distances are shown for each geometry. The bonds O_{ph}−C1 and O_{ph}− H_{ph} of phenol in the gas phase have calculated values of 1.376 and 0.973 Å, respectively.

O_{ph}−C1 and O_{ph}−H_{ph} bonds lengthened by 0.041−0.048 and 0.004−0.007 Å, respectively (O_{ph} and H_{ph} refer to the OH group of phenol). Upon interaction between O_{ph} and the metal atom, increments of 0.026, 0.035, and 0.036 Å were observed for the bonds Sc−O8, Fe−O8, and Ga−O8, respectively (the framework O8 atom was the closest to H_{ph} among the set binding the metal substituent). The O_{ph} remained at a distance of 2.239 Å from Sc, decreasing to 1.837 and 1.810 Å for Fe and Ga, respectively.

3.3. Dissociation of Phenol. We considered the dissociation of the O_{ph}−H_{ph} bond of phenol, followed by the transfer of H_{ph} to the closest framework O atom that bound the metal substituent, as the first step toward tautomerization (see Figure 8). After the dissociation, the strength of the binding free energies decreased by 7 and 9 kJ/mol for Sc and Ga, respectively, while increasing by 9 kJ/mol for Fe (by 4 kJ/ mol when considering the +U approach). The energy barriers of these processes remained below 40 kJ/mol, reaching a minimum of 33 kJ/mol for Sc and Fe (see Figure 8). In comparison, the activation energy on the Al-substituted T9 site has a value of 49 kJ/mol.[34] Similarly, the cleavage of the O_{ph}− H_{ph} bond of phenol has activation energies of 46 and 19 kJ/ mol on Pt(111) and Pd(111), respectively,[44] while the equivalent process in m-cresol shows values of 39 and 45 kJ/ mol on Pt(111) and Ru(0001).[19] This highlights the fact that the dissociation of phenol on three-coordinated Lewis acid sites at the external surface of zeolite MFI is as probable as on a range of extended metal surfaces.

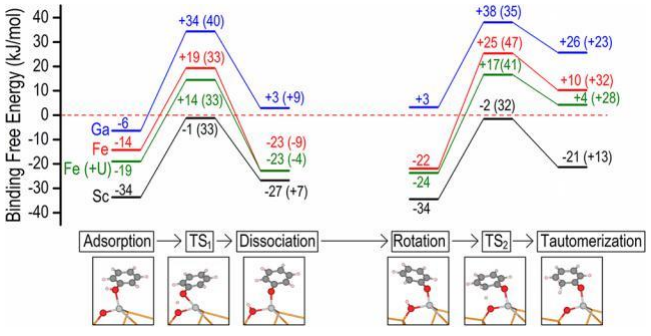

Figure 8. Binding free energies along the tautomerization pathway for the three Lewis centers: Sc (black line), Fe (red line), Fe with the +U correction (green), and Ga (blue line). The barrier and reaction energies for the dissociation of phenol (TS_1) and the formation of the final tautomer (TS_2) are shown within parentheses. The horizontal dashed line marks the reference energy (shifted to zero), constituted by the bare Lewis acid site and a molecule of phenol in the gas phase. Close-ups showing relevant structural features along the pathway are presented at the bottom of the graph. Important O atoms are represented in red, C atoms in dark gray, H atoms in white, metal substituent in light gray, and Si by orange sticks.

Figure 9 shows the optimized geometries of transition states (TS_1) and products of the dissociation of phenol for the

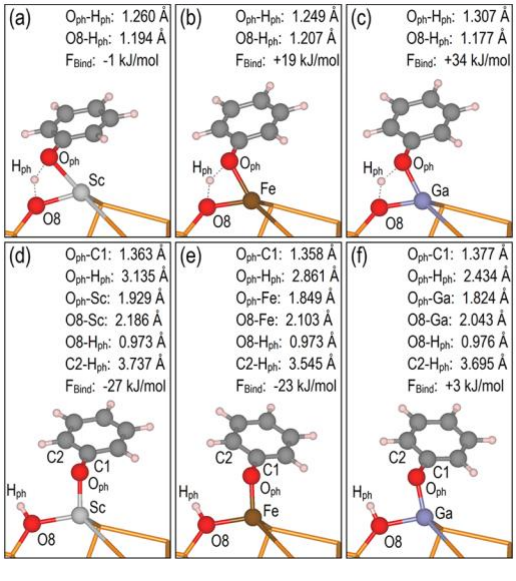

Figure 9. Optimized structures of (a−c) transition states (TS_1 in Figure 8) and (d−f) products of the dissociation of phenol using the coplanar configuration as input geometry: (a, d) Sc, (b, e) Fe, and (c, f) Ga. Important O atoms are represented in red, C atoms in dark gray, H atoms in white, and Si by orange sticks. Relevant interatomic distances are shown for each geometry.

different metal centers. In TS_1, H_{ph} was at an intermediate position between O_{ph} and O8, at no more than 1.31 Å away from either of the two O atoms. This range of distances was achieved by the movement of the phenol molecule toward the O8 atom, which shortened the O8−O_{ph} distance and distorted the metal-centered tetrahedron. After dissociation, the bond length O8−H_{ph} remained between 0.973 and 0.976 Å, which increased the distance between O8 and the metal substituents above 2.0 Å. As a consequence of the H_{ph} transfer, the O_{ph}−C1 bond was shortened by 0.047−0.061 Å, depending on the metal substituent.

3.4. Formation of Cyclohexa-2,4-dien-1-one. In order to complete the tautomerization, the dissociated phenol rotates around the dihedral angle C1−O_{ph}−M−O8 to decrease the distance between H_{ph} and C2, and to favor the transfer that produces the final tautomer. Previously, we have observed that this rotation has the lowest barrier along the tautomerization pathway with 12 kJ/mol.[34] The rotation avoids the regeneration of phenol by placing the molecule in an unfavorable orientation to retrieve H_{ph} from O8. Hence, we did not examine the value of the rotation barrier here, assuming it is also lower than the transfer of H_{ph} and we focused instead on the geometrical optimization of phenol upon rotation and formation of the tautomer.

Figure 10 shows the optimized geometries after the rotation of phenol around the dihedral angle C1−O_{ph}−M−O8. The

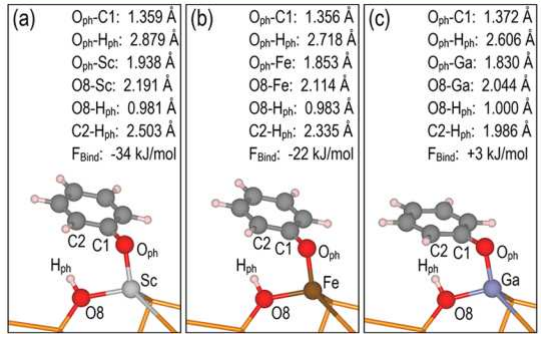

Figure 10. Optimized structures after the rotation of phenol around the dihedral angle C1−O_{ph}−M−O8 using the structures after the dissociation of phenol shown in Figure 9 as input geometries: (a) Sc, (b) Fe, and (c) Ga. Important O atoms are represented in red, C atoms in dark gray, H atoms in white, and Si by orange sticks. Relevant interatomic distances are shown for each geometry.

binding free energy strengthened by 7 kJ/mol for Sc while remaining unchanged for Fe and Ga. The distance C2−H_{ph} decreased to 2.503, 2.335, and 1.986 Å for Sc, Fe and Ga, respectively. These short separations between H_{ph} and the aromatic ring caused increments in the O8−H_{ph} bond by 0.008−0.024 Å (see Figure 10). We associated these increments with the perturbation that the electron-rich π cloud of phenol exerts on H_{ph}. We have observed a similar elongation of up to 0.031 Å for the O8−H_{ph} bond when the adsorption takes place on the three-coordinated Al-substituted T9 site.[34]

The final step of the tautomerization of phenol involves the breaking of the O8−H_{ph} bond and the H_{ph} transfer to C2, weakening the adsorption on the Lewis acid sites (see Figure 8). The binding free energy remained negative only for Sc, while increasing to +10 (+4 with the +U approach) and +25 kJ/mol for Fe and Ga, respectively. In the gas phase, the tautomer is highly unstable when compared to phenol, hence it should be stabilized on the Lewis site in order to span its lifetime long enough to go through further hydrogenation; in this regard, Sc is the best candidate among the three substitutions discussed here. The energy barrier for the transfer of H_{ph} to C2 showed the smallest value for Sc with 32 kJ/mol, followed by Ga and Fe with 35 and 47 kJ/mol, respectively. The inclusion of the +U correction on Fe decreased the barrier by only 6 kJ/mol compared to the noncorrected one, showing a value of 41 kJ/mol. On Sc, this activation energy is 5 kJ/mol larger than on Al, which is still

reachable at relatively low temperatures.[34] Likewise, the equivalent C−H_{ph} combination for phenol and m-cresol mediated by the metal surfaces Pt(111), Pd(111), and Ru(0001) has higher activation energies, with values ranging from 63 to 93 kJ/mol.[19,44] On these extended metallic surfaces, the H_{ph} atom and dissociated phenol are more strongly stabilized by multiple interactions with the surface metal atoms, which increases the energy of the C−H_{ph} bond formation compared to the zeolite Lewis acid sites, where only the highly polarized O8−H_{ph} bond needs to be broken.

Figure 11 shows the optimized geometries of transition states (TS_2) and products for the transfer of H_{ph} to C2. In the

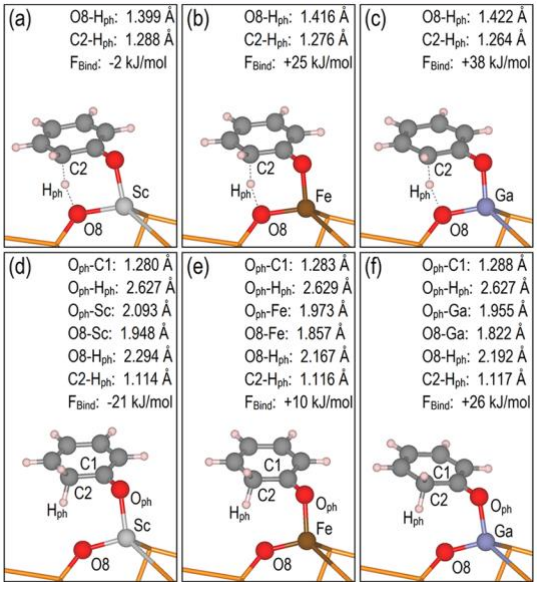

Figure 11. Optimized structures of (a−c) transition states (TS_2 in Figure 8) and (d−f) products of the final step of the tautomerization of phenol using the configurations shown in Figure 10 as input geometries: (a, d) Sc, (b, e) Fe, and (c, f) Ga. Important O atoms are represented in red, C atoms in dark gray, H atoms in white, and Si by orange sticks. Relevant interatomic distances are shown for each geometry.

TS_2, H_{ph} kept a distance from the C2 and O8 atoms between 1.26 and 1.42 Å for the three dopants (see Figure 11). Once the H_{ph} transfer was completed, the C2−H_{ph} bond length remained between 1.114 and 1.117 Å, and the O_{ph}−C1 bond reduced to values between 1.280 and 1.288 Å. These changes occurred together with an increase of the O_{ph}−M distance, with elongations of 0.155, 0.120, and 0.125 Å for Sc, Fe, and Ga, respectively.

According to the pathways summarized in Figure 8, the three metal substitutions are able to catalyze the tautomeriza-tion very effectively compared to the direct isomerization in the gas phase, which has an activation energy of 242 kJ/mol.[34] Our calculated activation energies for the tautomerization of phenol remained between 33 and 47 kJ/mol. Thus, the isomerization of phenol may be easily attainable on metal-substituted zeolites acting as supports. Although we have studied here substitutions with metal atoms with a formal charge of 3+, other Lewis acids with formal charge 4+ may also facilitate the tautomerization.[84]

The presence of other molecules, such as water, could assist the tautomerization of phenol in a single-step reaction instead of a three-step process as proposed here. For instance, the calculated energy barrier for the water-assisted tautomerization of phenol at the Ru−TiO_2(110) interphase is 37 kJ/mol, which is within the range of our calculated activation energies for the H_{ph} transfer.[43] We have not explicitly considered the effect of solvents on the tautomerization mechanism of phenol at the Lewis acid sites, but we could hypothesize that, once phenol is adsorbed on the Lewis acid site, water could facilitate the tautomerization by simultaneously accepting the phenol proton, while donating its own to one of the carbon atoms at ortho positions. This step would effectively reduce the activation energy of the hydrogen hopping.[91] However, this suggestion considers a single water molecule only, whereas more complex mechanisms could be devised by adding more molecules to the system.[92] Only the explicit treatment of the solvent would allow us to draw more specific conclusions. This is beyond the scope of the current study, but will be considered in future work.

4. CONCLUSIONS

We have performed density functional theory calculations in order to investigate the proficiency of three-coordinated Lewis acid sites in zeolite MFI to catalyze the tautomerization of phenol. The Lewis acid site was formed from the dehydration of the metal-substituted silanol group at the T9 site exposed at the external (010) surface of the zeolite. Three different metals, with formal charge 3+, were used to replace silicon in the T9 site: scandium, iron, and gallium. We have shown that phenol is able to substitute water on the Lewis site once the dehydration of the silanol group has taken place.

The tautomerization is conceived as a three-step process consisting of (i) dissociation of the O_{ph}−H_{ph} bond of phenol and the H_{ph} transfer to one of the framework O atoms binding the metal, (ii) rotation of the molecule to reduce the distance between the H_{ph} atom bound to the zeolite and one of the ortho C atoms of phenol, and (iii) transfer of the H_{ph} atom from the zeolite to the phenoxide to form the C−H_{ph} bond. The entire process has activation energies below 47 kJ/mol for any of the three dopants. In particular, the Sc gives the strongest binding free energy for phenol, the lowest activation energies during the tautomerization, and is the substituent that better stabilizes the final tautomer, followed by Fe and Ga. Furthermore, the three metals show a lower activation energy than Al for the first step of the tautomerization process, by 9 to 16 kJ/mol, although they simultaneously raise the barrier for the second H_{ph} transfer, with increments that range from 5 kJ/ mol for Sc to 20 kJ/mol for Fe (without +U correction). These results indicate that Sc could potentially be used as a dopant in zeolites with a promising performance to promote the tautomerization of phenol.

The utilization of the +U approach to describe the on-site Coulomb repulsion of the 3d electrons of Fe does not significantly modify quantitative results, which are mainly limited to the increase of the binding energy of phenol by no more than 10 kJ/mol. Finally, we have observed that the PBE functional is suitably accurate to describe the analyzed tautomerization pathway, compared to other functionals of higher hierarchy within the density functional theory, i.e., TPSS, rev-TPSS, and HSE06.

■ ASSOCIATED CONTENT

Binding energy of phenol on the Lewis acid site and energy barrier for the hydrogen transfer from phenol to the zeolite calculated by the functionals PBE, PBEsol, TPSS, rev-TPSS, and HSE06 and the electronic energy, thermal energy, enthalpy, entropy, and free energy of all chemical reactions reported in this work (PDF)

AUTHOR INFORMATION

Corresponding Author

*(N.H.d.L.) E-mail: deleeuwn@cardiff.ac.uk.

ORCID

Carlos Hernandez-Tamargo: 0000-0002-1413-5059

Nora H. de Leeuw: 0000-0002-8271-0545

Notes

The authors declare no competing financial interest.

ACKNOWLEDGMENTS

This work was performed using the computational facilities of the Advanced Research Computing @ Cardiff (ARCCA) Division, Cardiff University, and HPC Wales. Via our membership of the U.K.'s HEC Materials Chemistry Consortium, which is funded by EPSRC [grant number: EP/L000202], this work used the ARCHER UK National Supercomputing Service (http://www.archer.ac.uk). CEHT acknowledges EPSRC [grant number: EP/K009567/2] for funding and NHdL thanks the Royal Society for an Industry Fellowship. All data created during this research is openly available from the University of Cardiff Research Portal at http://doi.org/10.17035/d.2017.0031746452.

REFERENCES

(1) Rinaldi, R.; Schüth, F. Design of Solid Catalysts for the Conversion of Biomass. Energy Environ. Sci. 2009, 2, 610−626.

(2) Li, C.; Zhao, X.; Wang, A.; Huber, G. W.; Zhang, T. Catalytic Transformation of Lignin for the Production of Chemicals and Fuels. Chem. Rev. 2015, 115, 11559−11624.

(3) Ennaert, T.; Van Aelst, J.; Dijkmans, J.; De Clercq, R.; Schutyser, W.; Dusselier, M.; Verboekend, D.; Sels, B. F. Potential and Challenges of Zeolite Chemistry in the Catalytic Conversion of Biomass. Chem. Soc. Rev. 2016, 45, 584−611.

(4) Ben, H.; Ragauskas, A. J. Influence of Si/Al Ratio of ZSM-5 Zeolite on the Properties of Lignin Pyrolysis Products. ACS Sustainable Chem. Eng. 2013, 1, 316−324.

(5) Ma, Z.; Custodis, V.; Van Bokhoven, J. A. Selective Deoxygenation of Lignin during Catalytic Fast Pyrolysis. Catal. Sci. Technol. 2014, 4, 766−772.

(6) Mullen, C. A.; Boateng, A. A. Catalytic Pyrolysis-GC/MS of Lignin from Several Sources. Fuel Process. Technol. 2010, 91, 1446− 1458.

(7) Zhang, M.; Moutsoglou, A. Catalytic Fast Pyrolysis of Prairie Cordgrass Lignin and Quantification of Products by Pyrolysis-Gas Chromatography-Mass Spectrometry. Energy Fuels 2014, 28, 1066− 1073.

(8) Hong, D. Y.; Miller, S. J.; Agrawal, P. K.; Jones, C. W. Hydrodeoxygenation and Coupling of Aqueous Phenolics over Bifunctional Zeolite-Supported Metal Catalysts. Chem. Commun. 2010, 46, 1038−1040.

(9) Zhao, C.; Lercher, J. A. Selective Hydrodeoxygenation of Lignin-Derived Phenolic Monomers and Dimers to Cycloalkanes on Pd/C and HZSM-5 Catalysts. ChemCatChem 2012, 4, 64−68.

(10) Zhang, W.; Chen, J.; Liu, R.; Wang, S.; Chen, L.; Li, K. Hydrodeoxygenation of Lignin-Derived Phenolic Monomers and Dimers to Alkane Fuels over Bifunctional Zeolite-Supported Metal Catalysts. ACS Sustainable Chem. Eng. 2014, 2, 683−691.

(11) Kasakov, S.; Shi, H.; Camaioni, D. M.; Zhao, C.; Barath, E.; Jentys, A.; Lercher, J. A. Reductive Deconstruction of Organosolv Lignin Catalyzed by Zeolite Supported Nickel Nanoparticles. Green Chem. 2015, 17, 5079−5090.

(12) Singh, S. K.; Ekhe, J. D. Cu-Mo Doped Zeolite ZSM-5 Catalyzed Conversion of Lignin to Alkyl Phenols with High Selectivity. Catal. Sci. Technol. 2015, 5, 2117−2124.

(13) Wang, X.; Rinaldi, R. A Route for Lignin and Bio-Oil Conversion: Dehydroxylation of Phenols into Arenes by Catalytic Tandem Reactions. Angew. Chem., Int. Ed. 2013, 52, 11499−11503.

(14) Zhu, X.; Nie, L.; Lobban, L. L.; Mallinson, R. G.; Resasco, D. E. Efficient Conversion of m-Cresol to Aromatics on a Bifunctional Pt/ HBeta Catalyst. Energy Fuels 2014, 28, 4104−4111.

(15) Liu, H.; Jiang, T.; Han, B.; Liang, S.; Zhou, Y. Selective Phenol Hydrogenation to Cyclohexanone over a Dual Supported Pd-Lewis Acid Catalyst. Science 2009, 326, 1250−1252.

(16) Lu, J.; Behtash, S.; Mamun, O.; Heyden, A. Theoretical Investigation of the Reaction Mechanism of the Guaiacol Hydrogenation over a Pt(111) Catalyst. ACS Catal. 2015, 5, 2423−2435.

(17) Nie, L.; Resasco, D. E. Kinetics and Mechanism of m-Cresol Hydrodeoxygenation on a Pt/SiO2 Catalyst. J. Catal. 2014, 317, 22− 29.

(18) Nie, L.; De Souza, P. M.; Noronha, F. B.; An, W.; Sooknoi, T.; Resasco, D. E. Selective Conversion of m-Cresol to Toluene over Bimetallic Ni-Fe Catalysts. J. Mol. Catal. A: Chem. 2014, 388−389, 47−55.

(19) Tan, Q.; Wang, G.; Nie, L.; Dinse, A.; Buda, C.; Shabaker, J.; Resasco, D. E. Different Product Distributions and Mechanistic Aspects of the Hydrodeoxygenation of m-Cresol over Platinum and Ruthenium Catalysts. ACS Catal. 2015, 5, 6271−6283.

(20) De Souza, P. M.; Rabelo-Neto, R. C.; Borges, L. E. P.; Jacobs, G.; Davis, B. H.; Sooknoi, T.; Resasco, D. E.; Noronha, F. B. Role of Keto Intermediates in the Hydrodeoxygenation of Phenol over Pd on Oxophilic Supports. ACS Catal. 2015, 5, 1318−1329.

(21) Kokotailo, G. T.; Lawton, S. L.; Olson, D. H.; Meier, W. M. Structure of Synthetic Zeolite ZSM-5. Nature 1978, 272, 437−438.

(22) Jobic, H.; Tuel, A.; Krossner, M.; Sauer, J. Water in Interaction with Acid Sites in H-ZSM-5 Zeolite Does Not Form Hydroxonium Ions. A Comparison between Neutron Scattering Results and Ab Initio Calculations. J. Phys. Chem. 1996, 100, 19545−19550.

(23) Dedeček, J. J.; Sklenak, S.; Li, C.; Wichterlová, B.; Gabová, V.; Brus, J.; Sierka, M.; Sauer, J. Effect of Al-Si-Al and Al-Si-Si-Al Pairs in the ZSM-5 Zeolite Framework on the 27Al NMR Spectra. A Combined High-Resolution 27Al NMR and DFT/MM Study. J. Phys. Chem. C 2009, 113, 1447−1458.

(24) Sklenak, S.; Dedeček, J.; Li, C.; Wichterlová, B.; Gabová, V.; Sierka, M.; Sauer, J. Aluminium Siting in the ZSM-5 Framework by Combination of High Resolution 27Al NMR and DFT/MM Calculations. Phys. Chem. Chem. Phys. 2009, 11, 1237−1247.

(25) Hernandez-Tamargo, C. E.; Roldan, A.; De Leeuw, N. H. A Density Functional Theory Study of the Structure of Pure-Silica and Aluminium-Substituted MFI Nanosheets. J. Solid State Chem. 2016, 237, 192−203.

(26) Franke, M. E.; Sierka, M.; Simon, U.; Sauer, J. Translational Proton Motion in Zeolite H-ZSM-5. Energy Barriers and Jump Rates from DFT Calculations. Phys. Chem. Chem. Phys. 2002, 4, 5207− 5216.

(27) Tuma, C.; Sauer, J. A Hybrid MP2/Planewave-DFT Scheme for Large Chemical Systems: Proton Jumps in Zeolites. Chem. Phys. Lett. 2004, 387, 388−394.

(28) Tuma, C.; Sauer, J. Treating Dispersion Effects in Extended Systems by Hybrid MP2:DFT Calculations - Protonation of Isobutene in Zeolite Ferrierite. Phys. Chem. Chem. Phys. 2006, 8, 3955−3965.

(29) Tuma, C.; Sauer, J. Quantum Chemical Ab Initio Prediction of Proton Exchange Barriers between CH4 and Different H-Zeolites. J. Chem. Phys. 2015, 143, 102810.

(30) Hernandez-Tamargo, C. E.; Roldan, A.; De Leeuw, N. H. DFT Modeling of the Adsorption of Trimethylphosphine Oxide at the

Internal and External Surfaces of Zeolite MFI. J. Phys. Chem. C 2016, 120, 19097−19106.
(31) Davidová, M.; Nachtigallová, D.; Nachtigall, P.; Sauer, J. Nature of the Cu+-NO Bond in the Gas Phase and at Different Types of Cu+ Sites in Zeolite Catalysts. J. Phys. Chem. B 2004, 108, 13674−13682.
(32) Svelle, S.; Tuma, C.; Rozanska, X.; Kerber, T.; Sauer, J. Quantum Chemical Modeling of Zeolite-Catalyzed Methylation Reactions: Toward Chemical Accuracy for Barriers. J. Am. Chem. Soc. 2009, 131, 816−825.
(33) Piccini, G.; Alessio, M.; Sauer, J.; Zhi, Y.; Liu, Y.; Kolvenbach, R.; Jentys, A.; Lercher, J. A. Accurate Adsorption Thermodynamics of Small Alkanes in Zeolites. Ab Initio Theory and Experiment for H-Chabazite. J. Phys. Chem. C 2015, 119, 6128−6137.
(34) Hernandez-Tamargo, C. E.; Roldan, A.; de Leeuw, N. H. Density Functional Theory Study of the Zeolite-Mediated Tautomerization of Phenol and Catechol. Mol. Catal. 2017, 433, 334−345.
(35) Kosslick, H.; Tuan, V. A.; Parlitz, B.; Fricke, R.; Peuker, C.; Storek, W. Disruption of the MFI Framework by the Incorporation of Gallium. J. Chem. Soc., Faraday Trans. 1993, 89, 1131−1138.
(36) Li, J.; Miao, P.; Li, Z.; He, T.; Han, D.; Wu, J.; Wang, Z.; Wu, J. Hydrothermal Synthesis of Nanocrystalline H[Fe, Al]ZSM-5 Zeolites for Conversion of Methanol to Gasoline. Energy Convers. Manage. 2015, 93, 259−266.
(37) Briden, C. T.; Williams, C. D.; Apperley, D. A Study of the Chemistry of Isomorphous Substitution and Characterization of Al-ZSM-5 and Sc-ZSM-5 Synthesized in Fluoride Media. Inorg. Mater. 2007, 43, 758−769.
(38) Im, J.; Shin, H.; Jang, H.; Kim, H.; Choi, M. Maximizing the Catalytic Function of Hydrogen Spillover in Platinum-Encapsulated Aluminosilicates with Controlled Nanostructures. Nat. Commun. 2014, 5, 3370.
(39) Lee, S.; Lee, K.; Im, J.; Kim, H.; Choi, M. Revisiting Hydrogen Spillover in Pt/LTA: Effects of Physical Diluents Having Different Acid Site Distributions. J. Catal. 2015, 325, 26−34.
(40) Shin, H.; Choi, M.; Kim, H. A Mechanistic Model for Hydrogen Activation, Spillover, and Its Chemical Reaction in a Zeolite-Encapsulated Pt Catalyst. Phys. Chem. Chem. Phys. 2016, 18, 7035−7041.
(41) Hernandez-Tamargo, C. E.; Roldan, A.; Ngoepe, P. E.; De Leeuw, N. H. Periodic Modeling of Zeolite Ti-LTA. J. Chem. Phys. 2017, 147, 074701.
(42) Song, W.; Liu, Y.; Barath, E.; Zhao, C.; Lercher, J. A. Synergistic Effects of Ni and Acid Sites for Hydrogenation and C-O Bond Cleavage of Substituted Phenols. Green Chem. 2015, 17, 1204−1218.
(43) Nelson, R. C.; Baek, B.; Ruiz, P.; Goundie, B.; Brooks, A.; Wheeler, M. C.; Frederick, B. G.; Grabow, L. C.; Austin, R. N. Experimental and Theoretical Insights into the Hydrogen-Efficient Direct Hydrodeoxygenation Mechanism of Phenol over Ru/TiO2. ACS Catal. 2015, 5, 6509−6523.
(44) Li, G.; Han, J.; Wang, H.; Zhu, X.; Ge, Q. Role of Dissociation of Phenol in Its Selective Hydrogenation on Pt(111) and Pd(111). ACS Catal. 2015, 5, 2009−2016.
(45) Kresse, G.; Hafner, J. Ab Initio Molecular Dynamics for Liquid Metals. Phys. Rev. B: Condens. Matter Mater. Phys. 1993, 47, 558−561.
(46) Kresse, G.; Hafner, J. Ab Initio Molecular-Dynamics Simulation of the Liquid-Metal-Amorphous-Semiconductor Transition in Ger-manium. Phys. Rev. B: Condens. Matter Mater. Phys. 1994, 49, 14251− 14269.
(47) Kresse, G.; Furthmüller, J. Efficiency of Ab-Initio Total Energy Calculations for Metals and Semiconductors Using a Plane-Wave Basis Set. Comput. Mater. Sci. 1996, 6, 15−50.
(48) Kresse, G.; Furthmüller, J. Efficient Iterative Schemes for Ab Initio Total-Energy Calculations Using a Plane-Wave Basis Set. Phys. Rev. B: Condens. Matter Mater. Phys. 1996, 54, 11169−11186.
(49) Perdew, J. P.; Burke, K.; Ernzerhof, M. Generalized Gradient Approximation Made Simple. Phys. Rev. Lett. 1996, 77, 3865−3868.
(50) Perdew, J. P.; Ruzsinszky, A.; Csonka, G. I.; Vydrov, O. A.; Scuseria, G. E.; Constantin, L. A.; Zhou, X.; Burke, K. Restoring the Density-Gradient Expansion for Exchange in Solids and Surfaces. Phys. Rev. Lett. 2008, 100, 136406.
(51) Perdew, J. P.; Ruzsinszky, A.; Csonka, G. I.; Vydrov, O. A.; Scuseria, G. E.; Constantin, L. A.; Zhou, X.; Burke, K. Erratum: Restoring the Density-Gradient Expansion for Exchange in Solids and Surfaces [Phys. Rev. Lett. 100, 136406 (2008)]. Phys. Rev. Lett. 2009, 102, 039902.
(52) Tao, J.; Perdew, J. P.; Staroverov, V. N.; Scuseria, G. E. Climbing the Density Functional Ladder: Nonempirical Meta−generalized Gradient Approximation Designed for Molecules and Solids. Phys. Rev. Lett. 2003, 91, 146401.
(53) Perdew, J. P.; Ruzsinszky, A.; Csonka, G. I.; Constantin, L. A.; Sun, J. Workhorse Semilocal Density Functional for Condensed Matter Physics and Quantum Chemistry. Phys. Rev. Lett. 2009, 103, 026403.
(54) Heyd, J.; Scuseria, G. E.; Ernzerhof, M. Hybrid Functionals Based on a Screened Coulomb Potential. J. Chem. Phys. 2003, 118, 8207−8215.
(55) Heyd, J.; Scuseria, G. E.; Ernzerhof, M. Erratum: "Hybrid Functionals Based on a Screened Coulomb Potential" [J. Chem. Phys. 118, 8207 (2003)]. J. Chem. Phys. 2006, 124, 219906.
(56) Grimme, S. Semiempirical GGA-Type Density Functional Constructed with a Long-Range Dispersion Correction. J. Comput. Chem. 2006, 27, 1787−1799.
(57) Grimme, S.; Antony, J.; Ehrlich, S.; Krieg, H. A Consistent and Accurate Ab Initio Parametrization of Density Functional Dispersion Correction (DFT-D) for the 94 Elements H-Pu. J. Chem. Phys. 2010, 132, 154104.
(58) Grimme, S.; Ehrlich, S.; Goerigk, L. Effect of the Damping Function in Dispersion Corrected Density Functional Theory. J. Comput. Chem. 2011, 32, 1456−1465.
(59) Ambrosetti, A.; Alfè, D.; DiStasio, R. A.; Tkatchenko, A. Hard Numbers for Large Molecules: Towards Reliable Energetics for Supramolecular Systems. J. Phys. Chem. Lett. 2014, 5, 849−855.
(60) Kresse, G.; Joubert, D. From Ultrasoft Pseudopotentials to the Projector Augmented-Wave Method. Phys. Rev. B: Condens. Matter Mater. Phys. 1999, 59, 1758−1775.
(61) Blochl, P. E. Projector Augmented-Wave Method. Phys. Rev. B: Condens. Matter Mater. Phys. 1994, 50, 17953−17979.
(62) Ho, K. M.; Fu, C. L.; Harmon, B. N.; Weber, W.; Hamann, D. R. Vibrational Frequencies and Structural Properties of Transition Metals via Total-Energy Calculations. Phys. Rev. Lett. 1982, 49, 673− 676.
(63) Fu, C. L.; Ho, K. M. First-Principles Calculation of the Equilibrium Ground-State Properties of Transition Metals: Applica-tions to Nb and Mo. Phys. Rev. B: Condens. Matter Mater. Phys. 1983, 28, 5480−5486.
(64) Anisimov, V. I.; Korotin, M. A.; Zaanen, J.; Andersen, O. K. Spin Bags, Polarons, and Impurity Potentials in La2-XSrxCuO4 from First Principles. Phys. Rev. Lett. 1992, 68, 345−348.
(65) Dudarev, S. L.; Botton, G. A.; Savrasov, S. Y.; Humphreys, C. J.; Sutton, A. P. Electron-Energy-Loss Spectra and the Structural Stability of Nickel Oxide: An LSDA+U Study. Phys. Rev. B: Condens. Matter Mater. Phys. 1998, 57, 1505−1509.
(66) Santos-Carballal, D.; Roldan, A.; Grau-Crespo, R.; de Leeuw, N. H. First-Principles Study of the Inversion Thermodynamics and Electronic Structure of FeM2 × 4 (Thio)Spinels (M = Cr, Mn, Co, Ni; X = O, S). Phys. Rev. B: Condens. Matter Mater. Phys. 2015, 91, 195106.
(67) Wang, L.; Maxisch, T.; Ceder, G. Oxidation Energies of Transition Metal Oxides within the GGA+U Framework. Phys. Rev. B: Condens. Matter Mater. Phys. 2006, 73, 195107.
(68) Barta, K.; Warner, G. R.; Beach, E. S.; Anastas, P. T. Depolymerization of Organosolv Lignin to Aromatic Compounds over Cu-Doped Porous Metal Oxides. Green Chem. 2014, 16, 191− 196.
(69) Mills, G.; Jonsson, H.; Schenter, G. K. Reversible Work Transition State Theory: Application to Dissociative Adsorption of Hydrogen. Surf. Sci. 1995, 324, 305−337.

(70) Jonsson, H.; Mills, G.; Jacobsen, K. W. Nudged Elastic Band Method for Finding Minimum Energy Paths of Transitions. Classical and Quantum Dynamics in Condensed Phase Simulations 1997, 385− 404.
(71) Henkelman, G.; Jonsson, H. A Dimer Method for Finding Saddle Points on High Dimensional Potential Surfaces Using Only First Derivatives. J. Chem. Phys. 1999, 111, 7010−7022.
(72) Heyden, A.; Bell, A. T.; Keil, F. J. Efficient Methods for Finding Transition States in Chemical Reactions: Comparison of Improved Dimer Method and Partitioned Rational Function Optimization Method. J. Chem. Phys. 2005, 123, 224101.
(73) International Zeolite Association. (IZA) http://www.iza-online.org/ (accessed Jun 30, 2018).
(74) Birch, F. Finite Elastic Strain of Cubic Crystals. Phys. Rev. 1947, 71, 809−824.
(75) Francis, G. P.; Payne, M. C. Finite Basis Set Corrections to Total Energy Pseudopotential Calculations. J. Phys.: Condens. Matter 1990, 2, 4395−4404.
(76) Quartieri, S.; Arletti, R.; Vezzalini, G.; Di Renzo, F.; Dmitriev, V. Elastic Behavior of MFI-Type Zeolites: 3 - Compressibility of Silicalite and Mutinaite. J. Solid State Chem. 2012, 191, 201−212.
(77) Choi, M.; Na, K.; Kim, J.; Sakamoto, Y.; Terasaki, O.; Ryoo, R. Stable Single-Unit-Cell Nanosheets of Zeolite MFI as Active and Long-Lived Catalysts. Nature 2009, 461, 246−249.
(78) Bucko, T.; Benco, L.; Hafner, J. Defect Sites at the (001) Surface of Mordenite: An Ab Initio Study. J. Chem. Phys. 2003, 118, 8437−8445.
(79) Bucko, T.; Benco, L.; Demuth, T.; Hafner, J. Ab Initio Density Functional Investigation of the (001) Surface of Mordenite. J. Chem. Phys. 2002, 117, 7295−7305.
(80) Abril, D. M.; Slater, B.; Blanco, C. Modeling Dynamics of the External Surface of Zeolite LTA. Microporous Mesoporous Mater. 2009, 123, 268−273.
(81) Smirnov, K. S. A Modeling Study of Methane Hydrate Decomposition in Contact with the External Surface of Zeolites. Phys. Chem. Chem. Phys. 2017, 19, 23095−23105.
(82) Momma, K.; Izumi, F. VESTA 3 for Three-Dimensional Visualization of Crystal, Volumetric and Morphology Data. J. Appl. Crystallogr. 2011, 44, 1272−1276.
(83) Van Bokhoven, J. A.; Van der Eerden, A. M. J.; Koningsberger, D. C. Three-Coordinate Aluminum in Zeolites Observed with in Situ X-Ray Absorption near-Edge Spectroscopy at the Al K-Edge: Flexibility of Aluminum Coordinations in Zeolites. J. Am. Chem. Soc. 2003, 125, 7435−7442.
(84) Yang, G.; Zhou, L.; Han, X. Lewis and Brönsted Acidic Sites in M4+-Doped Zeolites (M = Ti, Zr, Ge, Sn, Pb) as Well as Interactions with Probe Molecules: A DFT Study. J. Mol. Catal. A: Chem. 2012, 363−364, 371−379.
(85) Bader, R. F. W.; Carroll, M. T.; Cheeseman, J. R.; Chang, C. Properties of Atoms in Molecules: Atomic Volumes. J. Am. Chem. Soc. 1987, 109, 7968−7979.
(86) Henkelman, G.; Arnaldsson, A.; Jonsson, H. A Fast and Robust Algorithm for Bader Decomposition of Charge Density. Comput. Mater. Sci. 2006, 36, 354−360.
(87) Sanville, E.; Kenny, S. D.; Smith, R.; Henkelman, G. Improved Grid-Based Algorithm for Bader Charge Allocation. J. Comput. Chem. 2007, 28, 899−908.
(88) Tang, W.; Sanville, E.; Henkelman, G. A Grid-Based Bader Analysis Algorithm without Lattice Bias. J. Phys.: Condens. Matter 2009, 21, 084204.
(89) Li, K.; Xue, D. Estimation of Electronegativity Values of Elements in Different Valence States. J. Phys. Chem. A 2006, 110, 11332−11337.
(90) Chorkendorff, I.; Niemantsverdriet, J. W. Concepts of Modern Catalysis and Kinetics, 2nd ed.; Wiley-VCH: Weinheim, Germany, 2007.
(91) Ryder, J. A.; Chakraborty, A. K.; Bell, A. T. Density Functional Theory Study of Proton Mobility in Zeolites: Proton Migration and Hydrogen Exchange in ZSM-5. J. Phys. Chem. B 2000, 104, 6998− 7011.
(92) Balta, B.; Aviyente, V. Solvent Effects on Glycine II. Water-Assisted Tautomerization. J. Comput. Chem. 2004, 25, 690−703.